This article has been accepted for publication in a future issue of this journal, but has not been fully edited. Content may change prior to final publication. Citation information: DOI 10.1109/TMECH.2017.2771763, IEEE/ASME Transactions on Mechatronics

Distributed Current Source Method for Modeling Magnetic and Eddy-Current Fields Induced in Non-Ferrous Metallic Objects

Chun-Yeon Lin, *Member, IEEE/ASME*, Kok-Meng Lee*, *Fellow, IEEE/ASME*, Bingjie Hao

***Abstract*— This paper presents a new modeling method to determine the harmonic eddy-current (EC) field induced in a non-ferrous metal and its corresponding magnetic flux density (MFD) by an EC-based sensing system for geometrical measurements, which accounts for the boundary effects of the object. Modeled using a distributed current source (DCS) method in state-space representation, the EC field is formulated as a two-step constrained least-square (CLS) problem to solve for its real and imaginary parts. Two practical techniques to improve the efficiency and accuracy of the EC solutions are illustrated; the first refines the DCS distribution based on the skin-depth effects, and the second takes advantages of commercial mesh-generation software to facilitate the modeling of EC induced in complex shaped objects. The DCS-based EC models are verified numerically by comparing computed results with 2D analytical axisymmetric solutions and commercial finite-element analysis (FEA), and evaluated experimentally with an EC sensor that measures the MFD generated by the induced EC in different materials and geometrical configurations.**

***Index Terms*—Eddy-current, displacement sensor, thickness measurement, modeling, skin depth**

I. Introduction

High performance measurement systems are increasingly in demand in modern manufacturing [1] where both geometrical precision and surface quality specifications of the workpiece must be met. As a non-contact sensing device capable of measuring various properties of the non-ferrous metal objects both statically and dynamically, eddy-current (EC) sensors are widely used in many applications due to their fast response, high sensitivity and harsh-environment workability. In manufacturing, EC devices have been employed in rapid mold surface heating [2], vibration suppression [3], and measurements of displacement [4][5], thickness [6][7][8], and electrical conductivity [8][9] that depends on temperature and is related to residual stress [10]. With few exceptions ([1] [6]), most existing eddy-current sensors rely on high-frequency excitation and base principles on single-output induction measurements. High-precision magnetic sensors with advantages of small size, fast response and low power consumption, which can fulfill measurement requirements at both high and low frequencies while ensuring compact structure integrity of the EC sensor, are now widely available at low cost. However, the potentials of EC sensors capable of multi-target measurements [1] are underexploited for intelligent manufacturing because the relationships between the geometrical/material parameters and measured magnetic fields are highly coupled and spatially nonlinear. For this reason, this paper presents an efficient, physically intuitive method for designing EC-based multi-target sensors and analyzing the effects of the geometrical/material properties being measured on the induced EC and its corresponding magnetic field.

Dodd *et al.* [10] derived an analytical model to calculate the eddy current induced by an annular coil in a plane. Recently, an analytical model to study the induced current and power loss of a thin conducting nonmagnetic plate of finite size was developed [12]. Jeng [13] numerically calculated the eddy current distribution of a 2D axisymmetric conducting slab with a flaw by separating the conductor to many rings. Theodoros *et al.* [14][15] proposed a truncated region eigenfunction expansion method to replace integral expressions for the axisymmetric electromagnetic field and impedance of the eddy current coil. In general, axisymmetric solutions assume idealized shapes to simplify derivations to obtain tractable solutions. Driven by the needs to simulate the induced eddy currents in biological tissues, the impedance method (IM) which subdivides the object into a number of cells was developed for transcranial magnetic stimulation (TMS); each cell is replaced by an equivalent impedance for calculation of power deposition by the eddy currents. This method was later extended to the independent impedance method (IIM) [16][17] to improve the conditionality and speed up the numerical convergences. The IM and IIM methods [18][19] account for the boundary effects but neglect mutual inductances because of the low electrical conductivity of biological tissues.

The analysis of EC devices often requires handling complex geometry in 3D space, which are solved numerically using methods such as finite-element analysis (FEA), boundary element method and mesh-free methods, offer an accurate (but a computationally demanding) means to predict the magnetic fields and induced eddy current from simple static to dynamic problems. To increase the size of the largest solvable problems for computing eddy currents in complicated electromagnetic systems, a hierarchical matrix with adaptive cross approximation for the boundary element methods based on stream functions was proposed in [20]. Besides these methods, a distributed multipole model (DMP) method was proposed in [21] to characterize the MFD fields of a permanent magnet (PM) or electromagnet (EM), and its extension equivalent-PM [22]. More recently, a similar but more general approach referred to here as a distributed current source (DCS) method was developed in [23], which derives closed-form solutions to model the magnetic and electric fields of an EM component.

This work was supported in part by the U. S. National Science Foundation under Grant CMMI-1662700 and EFRI-M3C-1137172, National Basic Research Program of China (973 Program Grant No. 2013CB035803).

Chun-Yeon Lin and Kok-Meng Lee are with the Woodruff Sch. of Mech. Eng. at Georgia Inst. of Tech., Atlanta, GA 30332-0405 USA,

Binjie Hao is with the State Key Lab. of Dig. Manuf. and Equip. Tech. (SKL-DMET), and Sch. of Mech. Sci. and Eng. at Huazhong Univ. of Sci. and Tech. (HUST), Wuhan, Hubei, 430074, P. R. China. Kok-Meng Lee is also Distinguished Professor of the SKL-DMET at HUST.

* *Corresponding author: Kok-Meng Lee (*kokmeng.lee@me.gatech.edu)

1083-4435 (c) 2017 IEEE. Personal use is permitted, but republication/redistribution requires IEEE permission. See http://www.ieee.org/publications_standards/publications/rights/index.html for more information.

This article has been accepted for publication in a future issue of this journal, but has not been fully edited. Content may change prior to final publication. Citation information: DOI 10.1109/TMECH.2017.2771763, IEEE/ASME Transactions on Mechatronics

Unlike FEA that requires a sufficiently large air space to enclose all the magnetic fields of both the EM and the EC to ensure its solution accuracy, the DCS method uses point sources to eliminate the air space. Motivated by the needs for a computationally-efficient model for measuring the eddy current and its magnetic field, Lee *et al.* [6] [24] developed an EC-based sensing method based on a material- independent model for simultaneously measuring the geometrical parameters (thickness and displacement) and electrical conductivity of a non-ferrous semi-infinite metallic workpiece. This paper relaxes several commonly made assumptions in modeling an EC field, and formulates a two-step constrained least-square (CLS) problem for solving the real and imaginary parts of an EC induced in a non-ferrous metallic object with a relatively complex geometry. Inspired by the flexible division algorithm [25] that divides the workspace geometrically into physics-governed elements, the EC and its MFD are formulated in state-space representation that has closed-form solutions. The remainder of this paper provides the following:

- Along with a constraint matrix that accounts for the geometrical boundary effects of the object and the continuity equation, a state-space model that characterizes the magnetic and eddy-current (M/EC) fields contributed by both the electromagnet (EM) and the conductor is formulated and numerically solved for the harmonic eddy-current density (ECD) induced in the conductive object.
- The DCS modeling method is numerically investigated and verified by comparing results with 2D analytical solutions and FEA simulations; both 2D and 3D configurations of a benchmark problem where a 2D annular electromagnet is perpendicular to a non-ferrous metallic plate are considered. As will be shown, tradeoffs between efficiency and accuracy can be achieved by appropriately distributing the current sources based on the skin-depth effects, particularly for materials with a high electrical conductivity and for the EC sensor operated at a very high frequency. Unlike FEA, the DCS method do not need to include air space in the computation of the ECD and MFD fields.
- The EC models and their applications are experimentally evaluated using a prototype EC sensor that houses a pair of single-axis MFD sensors. The experiments involve three materials (copper, aluminum and titanium), and three object configurations (namely, a semi-infinite conducting slab, an edge model and a plate with a through hole). As will be demonstrated, commercially available CAD and mesh generation software can be used to automate the grid assignments for computing the EC field induced in a geometrically complex object.

II. Formulation of ECD and its MFD

Figure 1 illustrates a typical eddy-current-density (ECD) sensor for geometrical measurements, and the parameters involved in its modeling. The conductor (and hence $\mathbf{r}_i$) is fixed relative to the EM; hence, the eddy-current (EC) is induced solely by a time-varying current flowing through the EM winding. In Fig. 1(a), the *xyz* coordinate frame is at the geometrical center of the EM with its Z-axis pointing away from the conductor along the axis. In the following discussion, the EM coil is assumed to consist of N_w turns wire (diameter d_w) through which an input current $I(t)$ flows with density $J(t)$ given in (1a) where C_E accounts for the fact that the current only passes through the circular wires:

$$J(t)=\frac{C_E}{a_o a}I(t) \text{ where } C_E=\frac{\pi}{\rho_a}\left[\frac{N_w D_w}{4(1-\rho_i)}\right]^2 \text{ and } D_w=\frac{d_w}{a_o} \tag{1a}$$

The characteristic geometrical parameters of the EM are normalized to its outer radius a_o and half-length a as follows:

$$\rho_i=\frac{a_i}{a_o};\ \rho_a=\frac{a}{a_o};\ H=\frac{h}{a};\ Z=\frac{z}{a} \text{ and } R=\frac{r}{a_o} \tag{1b~f}$$

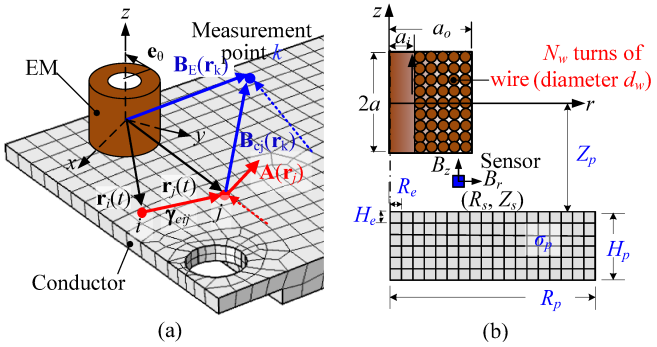

Fig. 1 Schematics showing variables/parameters used in modeling. (a) Conductor and EM in xyz coordinates. (b) 2D cylindrical coordinates.

The induced ECD (denoted as $\mathbf{J}(\in\mathbb{R}^{3\times1})=\mathbf{J}_E+\mathbf{J}_C$) is contributed by the time-varying magnetic fields of the EM and by the Conductor elements respectively, and can be explicitly expressed in terms of a geometry-dependent magnetic vector potential $\boldsymbol{\phi}(=\boldsymbol{\phi}_E+\boldsymbol{\phi}_C)$ using (A.3b) in Appendix. For the EM through which an uniform current density $J_E(t)$ flows,

$$\mathbf{J}_E(\mathbf{r}',t)=J_E(t)\mathbf{e}_\theta \text{ where } \mathbf{e}_\theta=-\sin\theta\mathbf{e}_x+\cos\theta\mathbf{e}_y \tag{2}$$

Using (A.2b) with $\frac{\mathbf{r}_j}{a_o}=\begin{bmatrix}R_j\cos\theta_j & R_j\sin\theta_j & \rho_a Z_j\end{bmatrix}^T$,

$$a_o^2\boldsymbol{\phi}_E(\mathbf{r}_j,t)=\mu_o\boldsymbol{\gamma}_E(\mathbf{r}_j)J_E(t) \tag{3}$$

In (3), $\boldsymbol{\gamma}_E(\mathbf{r}_j)$ depends on the winding geometry for a stationary EM (Fig. 1b):

$$\boldsymbol{\gamma}_E(\mathbf{r}_j)=aa_o\left(\frac{1}{4\pi}\int_{\theta=0}^{2\pi}\int_{Z=-1}^{1}\int_{R=\rho_i}^{1}\frac{\mathbf{e}_\theta}{|\mathbf{r}_j-\mathbf{r}'|/a_o}R\,dR\,dZ\,d\theta\right) \tag{4}$$

where $\frac{\mathbf{r}'}{a_o}=\begin{bmatrix}R\cos\theta & R\sin\theta & \rho_a Z\end{bmatrix}^T$.

For deriving practical ECD solutions, the conductor is decomposed into n hexahedron elements with their locations denoted by a displacement vector $\mathbf{r}_i(t)$ where i=1, 2, …, n. Each of the i^{th} element (volume v_i) is treated as an EC source with uniform density $\mathbf{J}_i$, electrical conductivity σ_i, and volume v_i. Using the distributed current source (DCS) method [23], $\boldsymbol{\phi}_C(\mathbf{r}_j)$ at location j can be similarly computed from the sum of the individual magnetic potential vectors contributed by the n elemental ECD sources $\mathbf{j}_i$ of the i^{th} conductor element:

$$a_o^2\boldsymbol{\phi}_C(\mathbf{r}_j)=\mu_o\sum_{i=1}^{n}\left(\gamma_{cji}v_i\right)\mathbf{j}_i \tag{5}$$

The modified kernel function γ_{cij} in (5), which accounts for the errors of the magnetic field computed around the current source with boundary r_{bi} [23] is given by (6):

1083-4435 (c) 2017 IEEE. Personal use is permitted, but republication/redistribution requires IEEE permission. See http://www.ieee.org/publications_standards/publications/rights/index.html for more information.

This article has been accepted for publication in a future issue of this journal, but has not been fully edited. Content may change prior to final publication. Citation information: DOI 10.1109/TMECH.2017.2771763, IEEE/ASME Transactions on Mechatronics

$$\gamma_{cij} \approx \frac{1}{4\pi}\begin{cases} 1/r_{ij} & i \neq j \\ \left(3r_{bi}^2 - r_{ij}^2\right)/\left(2r_{bi}^3\right) & i = j \end{cases} \text{ where } r_{ij} = \left|\mathbf{r}_j - \mathbf{r}_i\right|. \quad (6)$$

Using (3) and (5), which solve for the ECD induced by the EM and mutual inductances of the conductor, along (A.3b), the ECD source $\mathbf{j}_j$ in the j^{th} conductor element can be expressed in terms of the input current density J_E:

$$-\mathbf{j}_j = \mu_o\sigma_j \sum_{i=1}^{n}\left(\gamma_{cji} v_i \frac{d\mathbf{j}_i}{dt}\right) + \mu_o\sigma_j \boldsymbol{\gamma}_{\mathbf{E}j} \frac{dJ_E}{dt} \quad (7)$$

With $\mathbf{J}_\ell = \begin{bmatrix} j_{\ell 1} & \cdots & j_{\ell i} & \cdots & j_{\ell n} \end{bmatrix}^{\mathrm{T}}, \ell = x, y, z$ is defined as the state vector of the ℓ component ECD. $j_{\ell i}$ is the ℓ component ECD of the i_{th} element and $\dot{J}_E$ as an input. Equation (7) can be rewritten in state-space representation:

$$\dot{\mathbf{J}}_\ell = [\boldsymbol{\alpha}_1]\mathbf{J}_\ell + [\boldsymbol{\alpha}_2]\dot{J}_E \quad (8)$$

where $\boldsymbol{\alpha}_1 = -[\mathbf{A_C}]^{-1}[\mathbf{S}]^{-1}$; $\boldsymbol{\alpha}_2 = -[\mathbf{A_C}]^{-1}[\mathbf{A_E}]$;

$$\mathbf{A_C}(i,j) = v_j\gamma_{cij}(t) = v_j\gamma_{cji}(t);$$

$$[\mathbf{A_E}(t)] = \begin{bmatrix} \boldsymbol{\gamma}_{\mathbf{E}1} & \cdots & \boldsymbol{\gamma}_{\mathbf{E}j} & \cdots & \boldsymbol{\gamma}_{\mathbf{E}n} \end{bmatrix}^{\mathrm{T}};$$

and $a_o^{-2}[\mathbf{S}] = diag\left(\mu_o\sigma_1 \cdots \mu_o\sigma_j \cdots \mu_o\sigma_n\right)$.

The MFD at any point k in the neighborhood of the conductor, which is denoted as $\mathbf{B}(\mathbf{r}_k, t)$, is a combination of the MFDs contributed by the EM and the EC, $\mathbf{B}=\mathbf{B}_E+\mathbf{B}_C$ where $\mathbf{B}$ is directly measured; and $\mathbf{B}_E$ due to the current flowing through the EM (Fig. 1b):is real and can be pre-calibrated. The MFD contributed by the eddy-current is given by the output equation:

$$\mathbf{B}(\mathbf{r}_k, t) - \mathbf{B}_\mathbf{E} = \frac{\mu_0}{4\pi}[\mathbf{J_S}(t)][\mathbf{V_S}]\mathbf{R}_k(\mathbf{r}_k) \quad (9)$$

where $\mathbf{B}_\mathbf{E} = \boldsymbol{\eta}_\mathbf{E}(\mathbf{r}_k)J_E(t)$ (10a)

In (10a), $\boldsymbol{\eta}_E(\mathbf{r}_k)$ depends on the winding geometry:

$$\boldsymbol{\eta}_\mathbf{E}(\mathbf{r}_k) = a\left(\frac{\mu_o}{4\pi}\int_{\theta=0}^{2\pi}\int_{Z=-1}^{1}\int_{R=\rho_i}^{1}\frac{\mathbf{e_0}\times(\mathbf{r}_k - \mathbf{r}')}{\left|\mathbf{r}_k - \mathbf{r}'\right|^3} R\,dR\,dZ\,d\theta\right)$$

The term on the right side of (9) accounts for the mutual inductance of among the conductor elements, where

$$[\mathbf{J_S}(t)] = \left[skew(\mathbf{J}_1(t)) \cdots skew(\mathbf{J}_i(t)) \cdots skew(\mathbf{J}_n(t))\right]; \quad (10b)$$

$$[\mathbf{V_S}] = diag\left(v_1\mathbf{I} \quad \cdots \quad v_i\mathbf{I} \quad \cdots \quad v_n\mathbf{I}\right); \quad (10c)$$

$$\mathbf{R}_k = \begin{bmatrix} \mathbf{r}_{1k}^{\mathrm{T}}/r_{1k}^3 & \cdots & \mathbf{r}_{ik}^{\mathrm{T}}/r_{ik}^3 & \cdots & \mathbf{r}_{nk}^{\mathrm{T}}/r_{nk}^3 \end{bmatrix}^{\mathrm{T}}. \quad (10d)$$

and $skew(\mathbf{J_i}) = \begin{bmatrix} 0 & -J_{iz} & J_{iy} \\ J_{iz} & 0 & -J_{ix} \\ -J_{iy} & J_{ix} & 0 \end{bmatrix}$ (10e)

In state-space representation, (8) and (9) are the state and output equations of the EM/Conductor system (Fig. 1) respectively. Equations (4) and (10a) are presented in full forms for establishing a relatively complete state-space formulation with accurate solutions for future benchmark comparison. Once understood, approximated closed-form solutions (such as [6] [21]) could be developed within the framework for real-time computing.

A. Constraints imposed on the governing equations of ECD

To obtain solutions that uniquely describe the system (Fig. 1), (8) must satisfy the principle of conservation of charge, and account for the physically meaningful boundary conditions. For simplicity in illustration, Fig. 2(a) shows a hexahedron element is characterized by three orthogonal vectors $\mathbf{u}_\ell$ and six surfaces $s_{\ell\pm}$ and their normal $\mathbf{n}_{\ell\pm}$ where the subscript "±"indicates the "+" or "–" side along the $\ell = x$, y or z axis. The surface areas and surface-normal vectors of the i^{th} element can be mathematically written as (11a~f):

$$s_{ix\pm} = \left|\mathbf{u}_{iy+}\times\mathbf{u}_{iz\pm}\right|;\ s_{iy\pm} = \left|\mathbf{u}_{iz+}\times\mathbf{u}_{ix\pm}\right|;\ s_{iz\pm} = \left|\mathbf{u}_{ix+}\times\mathbf{u}_{iy\pm}\right| \quad (11a\sim c)$$

$$\mathbf{n}_{ix\pm} = \frac{\mathbf{u}_{iy+}\times\mathbf{u}_{iz\pm}}{s_{ix\pm}};\ \mathbf{n}_{iy\pm} = \frac{\mathbf{u}_{iz+}\times\mathbf{u}_{ix\pm}}{s_{iy\pm}};\ \mathbf{n}_{iz\pm} = \frac{\mathbf{u}_{ix+}\times\mathbf{u}_{iy\pm}}{s_{iz\pm}}. \quad (11d\sim f)$$

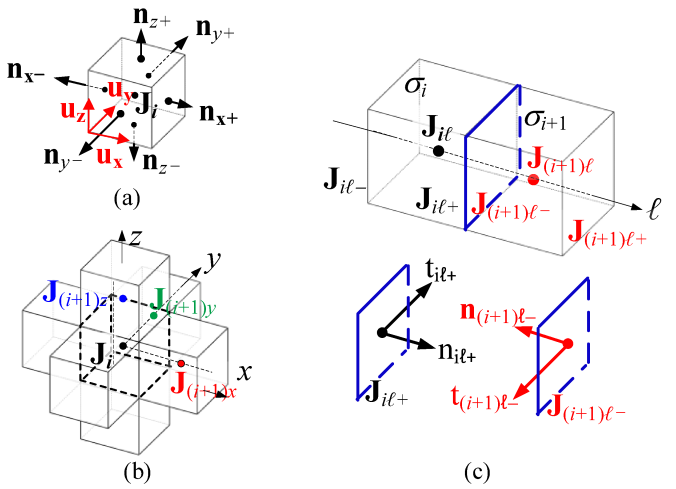

Fig. 2 Schematics illustrating the symbols for describing constraints. (a) Hexahedron element. (b) Connected elements. (c) Interface between i and i+1.

Conservation law

The steady ECD must satisfy the continuity equation, $\nabla\cdot\mathbf{J} = 0$ can be written in integral form using the divergence theorem to satisfy the conservation law for a hexahedron element. Numerically, the algebraic sum of the outward-flowing eddy-current of the i^{th} element is zero:

$$\sum_{k=1}^{6} s_k\left(\mathbf{J}_{ik}\bullet\mathbf{n}_k\right) = 0 \quad (12)$$

In (12), the subscript k (=1, …6) corresponds to the surfaces (x+, x–, y+, y–, z+, z–); s_k and $\mathbf{n}_k$ are defined in (11a,b). For computing (8), the ECD $\mathbf{J}_{ik}$ at the six surfaces (Fig. 2b) can be computed using the forward finite-difference:

$$\mathbf{J}_{i\ell-} = \mathbf{J}_i \text{ and } \mathbf{J}_{i\ell+} = \mathbf{J}_{(i+1)\ell} \quad (13a,b)$$

Boundary conditions

When the ECD obliquely crosses an interface between two media with different conductivities, the ECD vector changes both in direction and in magnitude. The steady ECD is divergence-less and curl-free and thus satisfies two conditions; 1) the normal component $\mathbf{n}$ of a divergenceless vector field is continuous; and 2) the tangential component $\mathbf{t}$ of a curl-free vector field is continuous across an interface. With the aid of Fig. 2(c), they are given in (14a) and (14b) respectively:

1083-4435 (c) 2017 IEEE. Personal use is permitted, but republication/redistribution requires IEEE permission. See http://www.ieee.org/publications_standards/publications/rights/index.html for more information.

This article has been accepted for publication in a future issue of this journal, but has not been fully edited. Content may change prior to final publication. Citation information: DOI 10.1109/TMECH.2017.2771763, IEEE/ASME Transactions on Mechatronics

$$\mathbf{J}_{i\ell+} \bullet \mathbf{n}_{i\ell+} = \mathbf{J}_{(i+1)\ell-} \bullet \mathbf{n}_{(i+1)\ell-} \tag{14a}$$

$$\sigma_{i\ell+}\left(\mathbf{J}_{(i+1)\ell-} \bullet \mathbf{t}_{(i+1)\ell-}\right) = \sigma_{(i+1)\ell-}\left(\mathbf{J}_{i\ell+} \bullet \mathbf{t}_{i\ell+}\right) \tag{14b}$$

where $\mathbf{n}_\ell + \mathbf{t}_\ell = \mathbf{1}$.

Thus, the constraint matrix [**Q**] consists of [$\mathbf{Q}_C$] accounting for the conservation law and ([$\mathbf{Q}_{Bn}$], [$\mathbf{Q}_{Bt}$]) for the constraints imposed on the boundary surfaces in the (normal, tangential) directions respectively. For n elements with a total of m boundary surfaces,

$$[\mathbf{Q}]\left(\in \mathbb{R}^{(n+2m)\times 3n}\right) = \left[[\mathbf{Q}_C]^{\mathrm{T}} \quad [\mathbf{Q}_{Bn}]^{T} \quad [\mathbf{Q}_{Bt}]^{\mathrm{T}}\right]^{\mathrm{T}} \tag{15}$$

where $[\mathbf{Q}_C] \in \mathbb{R}^{n\times 3n}$, $[\mathbf{Q}_{Bn}] \in \mathbb{R}^{m\times 3n}$ and $[\mathbf{Q}_{Bt}] \in \mathbb{R}^{m\times 3n}$.

To facilitate implementation, the elements in the i^{th} row of the constraint matrices ($[\mathbf{Q}_C]$, $[\mathbf{Q}_{Bn}]$, $[\mathbf{Q}_{Bt}]$) are given in (16a~c) using the selection vector $\mathbf{b}_{ik\ell}$ define in (16d) where the subscripts k and ℓ refer to the six surfaces and three axes of the i^{th} element:

$$\mathbf{Q}_{Ci}(\in \mathbb{R}^{1\times 3n}) = \sum_{k=1}^{6} s_{ik} \sum_{\ell=x,y,z} n_{ik\ell}\mathbf{b}_{ik\ell} \tag{16a}$$

$$\mathbf{Q}_{Bni} = \sum_{\ell=x,y,z}\left[n_{i\ell+}\mathbf{b}_{i\ell+} - n_{(i+1)\ell-}\mathbf{b}_{(i+1)\ell-}\right] \tag{16b}$$

$$\mathbf{Q}_{Bti} = \sum_{\ell=x,y,z}\left[2\Delta_{i\ell+}^{-2}t_{(i+1)\ell-}\mathbf{b}_{(i+1)\ell-} - \Delta_{(i+1)\ell-}^{-2}t_{i\ell+}\mathbf{b}_{i\ell+}\right] \tag{16c}$$

$$\mathbf{b}_{ik\ell}\left(\in \mathbb{R}^{1\times 3n}\right) = \begin{cases} 1 & \text{at } k \text{ surface along } \ell \text{ axis} \\ 0 & \text{else} \end{cases} \tag{16d}$$

A surface is defined as a boundary surface if it belongs only to a hexahedron element or an inner surface if it belongs to two hexahedron elements. Each element takes a row of [$\mathbf{Q}_C$] and each boundary surface takes one row of [$\mathbf{Q}_{Bn}$] and [$\mathbf{Q}_{Bt}$].

B. Harmonic solutions to the ECD and its generated MFD

When a sinusoidal current density $J_E(t) = J_o e^{j\omega t}$ flows through an annular electromagnet (EM) which generates a magnetic flux density (MFD), the steady state ECD $\mathbf{J}e^{j\omega t}$ (where $\mathbf{J} = \mathbf{J}_{\mathrm{Re}} + j\mathbf{J}_{\mathrm{Im}}$ with the subscripts "Re" and "Im" denoting the real and imaginary parts respectively) is induced in the non-ferrous electric conductive plate placed below the EM. J_0 is the current density of the EM, which can be determined by (1a). For a harmonic input $I_o e^{j\omega t}$, the time derivatives of the input current density and induced ECD are $\left(\dot{J}_E, \dot{\mathbf{J}}\right) = j\omega\left(J_E, \mathbf{J}\right)$ and ω is the angular frequency. The (Re, Im) parts of the ℓ (= x, y, z) components, $\left(\mathbf{J}_{\ell\mathrm{Re}}, \mathbf{J}_{\ell\mathrm{Im}} \in \mathbb{R}^{n\times 1}\right)$ can be solved from (8) in terms the skin-depth δ normalized to the outer radius a_o of the EM as shown in (17) where the subscript j is the element number to account for any material variation within the non-ferrous metal (with the relative magnetic permeability μ_r equal to 1):

$$\Delta_j = \frac{\delta_j}{a_o} \text{ where } \delta_j = \sqrt{\frac{2}{\omega\sigma_j\mu_o\mu_r}} \tag{17}$$

In (17), σ_j is the electrical conductivity and μ_o (=$4\pi\times10^{-7}$H/m) is the magnetic permeability of free space. The steady-state harmonic solutions to (8) are given by (18a,b) in terms of a normalized skin-depth (introduced here to derive a unified solution independent of materials):

$$\mathbf{J}_{\ell\mathrm{Re}} = \left[\bar{\mathbf{S}}\right]\left[\mathbf{A}_C\right]\mathbf{J}_{\ell\mathrm{Im}} \tag{18a}$$

where $\left[\bar{\mathbf{S}}\right] = diag\left(2\Delta_1^{-2}\cdots \quad 2\Delta_j^{-2} \quad \cdots 2\Delta_n^{-2}\right)$.

$$\mathbf{J}_{\ell\mathrm{Im}} = J_E\ \mathbf{E}_\ell \tag{18b}$$

where $\mathbf{E}_\ell = -\left[\mathbf{I} + \left(\left[\bar{\mathbf{S}}\right]\left[\mathbf{A}_C\right]\right)^2\right]^{-1}\left[\bar{\mathbf{S}}\right]\boldsymbol{\phi}_{\mathbf{E}\ell}$.

The ECD in the conductive plate is formulated as a two-step constrained least-square (CLS) problem: The first CLS solves (18b) for $\mathbf{J}_{\mathrm{Im}} = \left[\mathbf{J}_{x\mathrm{Im}}^{\mathrm{T}} \quad \mathbf{J}_{y\mathrm{Im}}^{\mathrm{T}} \quad \mathbf{J}_{z\mathrm{Im}}^{\mathrm{T}}\right]^{\mathrm{T}}$ by minimizing

$$\sum_{\ell=x,y,z}\left\|\mathbf{J}_{\ell\mathrm{Im}} - \mathbf{E}_\ell J_E\right\|^2 \text{ subject to } [\mathbf{Q}]\mathbf{J}_{\mathrm{Im}} = 0 \tag{19}$$

With $\mathbf{J}_{\mathbf{I}}$, the second CLS solves (18a) for $\mathbf{J}_{\mathrm{Re}} = \left[\mathbf{J}_{x\mathrm{Re}}^{\mathrm{T}} \quad \mathbf{J}_{y\mathrm{Re}}^{\mathrm{T}} \quad \mathbf{J}_{z\mathrm{Re}}^{\mathrm{T}}\right]^{\mathrm{T}}$ by minimizing

$$\sum_{\ell=x,y,z}\left\|\mathbf{J}_{\ell\mathrm{Re}} - \left[\bar{\mathbf{S}}\right]\left[\mathbf{A}_C\right]\mathbf{J}_{\ell\mathrm{Im}}\right\|^2 \text{ subject to } [\mathbf{Q}]\mathbf{J}_{\mathrm{Re}} = 0 \tag{20}$$

In (19) and (20), $\ell = x,\ y, z$ and $\mathbf{J}_{\ell\mathrm{Re}}, \mathbf{J}_{\ell\mathrm{Im}} \in \mathbb{R}^{n\times 1}$.

The measured MFD at any point k in the neighborhood of the conductor, which is denoted as $\mathbf{B}(\mathbf{r}_k, t) = \left[\mathbf{B}_{\mathrm{Re}} \quad \mathbf{B}_{\mathrm{Im}}\right]^{\mathrm{T}}$, where $\mathbf{B}_{\mathrm{Re}}, \mathbf{B}_{\mathrm{Im}}$ are combinations of MFDs. $\mathbf{B}_E$ generates from the EM, and can be pre-calibrated. The output equation (9) can be computed from (21) where $\left[\mathbf{J}_{\mathbf{S}\mathrm{Re}}\right]$ and $\left[\mathbf{J}_{\mathbf{S}\mathrm{Im}}\right]$ are the real and imaginary parts of $\mathbf{J}_{\mathbf{S}}$ (10b):

$$\begin{bmatrix} \mathbf{B}_{\mathrm{Re}} - \mathbf{B}_{\mathbf{E}} \\ \mathbf{B}_{\mathrm{Im}} \end{bmatrix} = \frac{\mu_o}{4\pi}\begin{bmatrix} \left[\mathbf{J}_{\mathbf{S}\mathrm{Re}}\right]\left[\mathbf{V}_{\mathbf{s}}\right]\mathbf{R}_k\left(\mathbf{r}_k\right) \\ \left[\mathbf{J}_{\mathbf{S}\mathrm{Im}}\right]\left[\mathbf{V}_{\mathbf{s}}\right]\mathbf{R}_k\left(\mathbf{r}_k\right) \end{bmatrix} \tag{21}$$

III. Numerical Illustration and Verifications

The DCS method and its physical insights for modeling an EM-induced ECD field are best illustrated numerically and verified by comparing with published 2D analytical solutions [10] for a coil above a semi-infinite conducting slab and FEA-simulated results. For an axisymmetric configuration where the magnetic vector potential and induced ECD only exist in the tangential direction, the continuity equation (13a,b) and boundary constraints (14a,b) are automatically satisfied. The ECD solutions (8) reduce to 2D, where v_j is replaced by an elemental area c_j; and the modified kernel function γ_{cij} that accounts for the 2D simplification is given by

$$\gamma_{cij} = \frac{1}{4\pi}\int_0^{2\pi}\frac{\cos\theta}{f(\theta)}d\theta \text{ where } f(\theta) = \begin{cases} 2\left(R - \cos\theta\right) & i = j \\ \left|\mathbf{r}_j - \mathbf{r}'\right| / a_o & i \neq j \end{cases} \tag{22}$$

Three sets of numerical investigations were performed. The *first* set simulates the skin-depth effect on flexible grid division that refines the grid distribution based on equal current densities. The *second* set investigates the boundary effects on the computed ECD field where the analytical (2D axisymmetric) solutions [10] provide a basis for comparison. The *third* numerically evaluates the DCS method and its effectiveness (computational efficiency and accuracy) by comparing results with FEA in both 2D and 3D.

1083-4435 (c) 2017 IEEE. Personal use is permitted, but republication/redistribution requires IEEE permission. See http://www.ieee.org/publications_standards/publications/rights/index.html for more information.

This article has been accepted for publication in a future issue of this journal, but has not been fully edited. Content may change prior to final publication. Citation information: DOI 10.1109/TMECH.2017.2771763, IEEE/ASME Transactions on Mechatronics

A. *Flexible grid division based on equal current*

Without loss of generality, an axisymmetric configuration is used as an example in Fig. 3 to illustrate a grid refinement method that takes into account the skin-depth effect on the ECD solutions. The method resizes the divisions such that all the elements have equalized current density as compared in Figs. 3(a) and 3(d), which show the initially uniform and refined grids respectively. The method is illustrated in Figs. 3(b) and 3(c), where the probability density function (PDF) is defined as the summation of the ECDs along the depth for a specific radius or the radius for a pre-determined depth; and the cumulative distribution function (CDF) is the accumulated PDF in corresponding direction. Fig. 3(b) plots the PDF and its corresponding CDF of the ECD magnitude normalized to its maximum magnitude ($|J|/J_{Max}$) in the radial direction. Similarly, Fig. 3(c) plots the PDF and CDF but in the Z direction. The refined (R, Z) grid lines on the conductor (Fig. 3d) represent an even distribution of the ECD magnitudes along the (R,Z) directions, which can be obtained through the projection of the equalized divided current-densities on the CDF(R) and CDF(Z) as illustrated in Figs. 3(b) and 3(c).

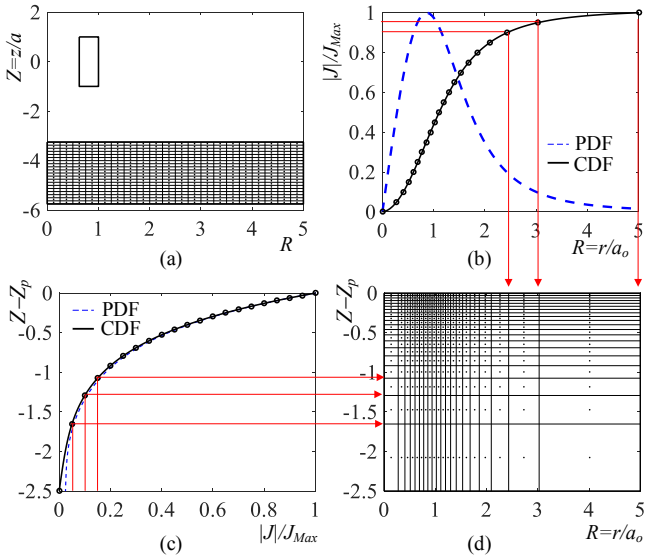

Fig. 3 Grid refinement method. (a) Uniform grids. (b) PDF(R), CDF(R). (c) PDF(Z), CDF(Z). (d) Refined grids.

To help visualization, Figs. 4(a~c) show the effects of the normalized skin-depth Δ and the plate-to-coil width aspect ratio R_p(=r_p/a_o) on CDF(Z) and CDF(R). Smaller skin depth (Δ) and larger R_P causes that the ECD distribution is more non-uniform in Z and R directions. Smaller Δ leads to the ECDs more concentrate near the surface, and larger R_p makes the ECDs concentrate near the EM and sparse on the edge.

As shown in Figs. 4(a) where R_p=2, the ECD concentrates more on the surface with smaller Δ, and is relatively insensitive to Δ in the R direction. On the other hand, R_p has a significant influence on the CDF(R) but negligible effects on CDF(Z) as compared in Fig. 4(b) for a given Δ=1; thus, the ECD distributes more uniformly with a smaller R_p but abruptly changes near the EM when R_p >5. The above parametric effects on the grid divisions can be visually seen in Fig. 4(c) where the horizontal axis R is graphed in $\log_{10}$ scale for clarity, and starts from 0+ to avoid taking $\log_{10}$ of R=0. Fig. 4(c) shows that the ECD concentrates near the coil edge (R=1) in the R direction, and denser grids in the (Z–Z_p) direction are needed near the surface with smaller Δ. The case (Δ=0.2, R_p=2) requires finer grids near the surface while uniform grids are sufficient for (Δ=1, R_p=2). Similarly, the case (Δ=1, R_p=20) requires finer grids below the EM but uniform along Z direction, whereas the case (Δ=0.2, R_p=20) requires both a much denser grids directly below the EM and near the surface.

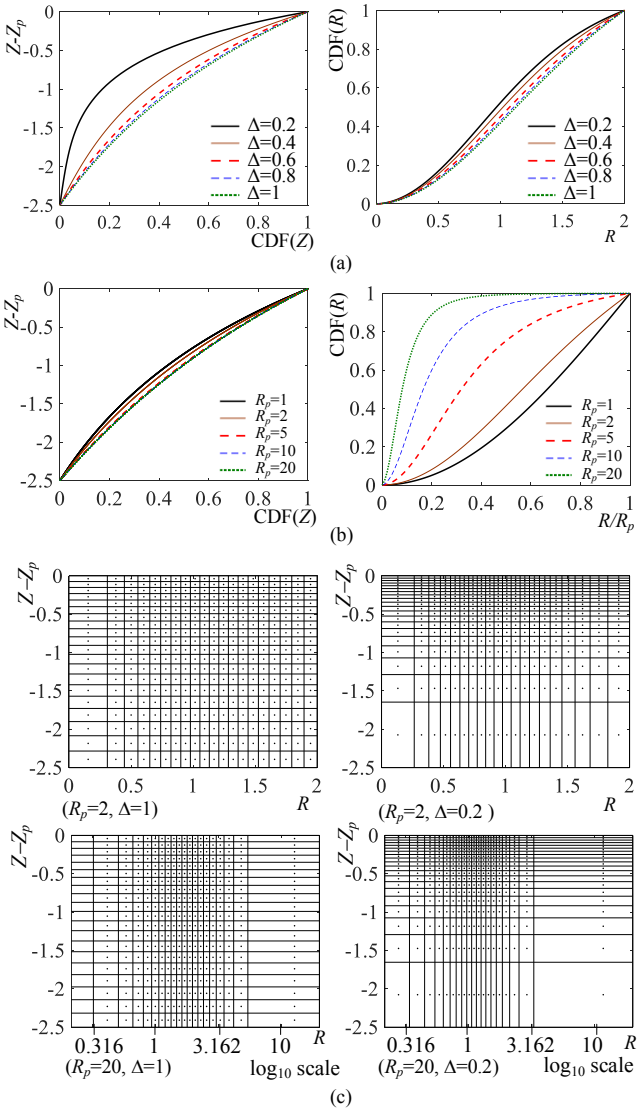

Fig. 4 Parametric effects of grid divisions (H_p=2.5, Z_p=3.25). (a) Effect of normalized skin-depth Δ on CDF (R_p=2). (b) Effect of the plate-to-coil aspect ratio on CDF (Δ=1). (c) Effect of skin-depth plate-to-coil aspect ratio on grid divisions.

A general method that takes advantages of commercial CAD and mesh generation software to model the EC field induced in a geometrically complex object is outlined in Appendix B and will be illustrated experimentally in Section IV.

B. *Axisymmetric ECD distribution and boundary effects*

Figure 5(a) shows the real and imaginary parts of the ECD fields induced in the circular plate (characterized by thickness H_p=2.5 and located at Z_p = 2.75 below the EM), which were numerically computed using (19) and (20) along the R direction at Z = −5. Figs. 5(b, c) graph the real and imaginary parts of the tangential ECD at different R and Z locations. The parametric

1083-4435 (c) 2017 IEEE. Personal use is permitted, but republication/redistribution requires IEEE permission. See http://www.ieee.org/publications_standards/publications/rights/index.html for more information.

This article has been accepted for publication in a future issue of this journal, but has not been fully edited. Content may change prior to final publication. Citation information: DOI 10.1109/TMECH.2017.2771763, IEEE/ASME Transactions on Mechatronics

values that characterize the EM and the normalized skin-depth Δ are given in the first row of Table I. The boundary effects on the ECD models can be analyzed by investigating the effect of different radii on the computed tangential ECD; (R_p=r_p/a_o=1, 2 and 3) in Fig. 5(a) and (R_p = 5) in Fig. 5(b, c). In Fig. 5, the analytical solutions [10] (solid-line curves) provide a basis for comparison. The DCS model and the analytical solutions agree well for $R_p \geq 3$ but the discrepancy increases for smaller R_p as shown in Fig. 5(a). Unlike the 2D analytical solutions that yield a single pair of (real and imaginary) curves regardless of R_p, the DCS model accounts for the boundary effects.

TABLE I. SIMULATION PARAMETRIC VALUES

EM, Δ = 0.7926	(a_o, a) = (6, 2) mm, ρ_i = 0.625; J_0 = 4.276 A/mm^2,			
Method	**DCS 2D**	**DCS 3D**	**FEA 2D**	**FEA 3D**
Elements	360	1,296	2,630	120,529
MFD (G) at (R_s=0, Z_s=4.5)	$\|B_r\|$=0 $\|B_z\|$=20.26	$\|B_x\|$=0.026 $\|B_y\|$=0.026 $\|B_z\|$=20.24	$\|B_r\|$≈0.037 $\|B_z\|$=20.17	$\|B_x\|$=0.048 $\|B_y\|$=0.209 $\|B_z\|$=20.24

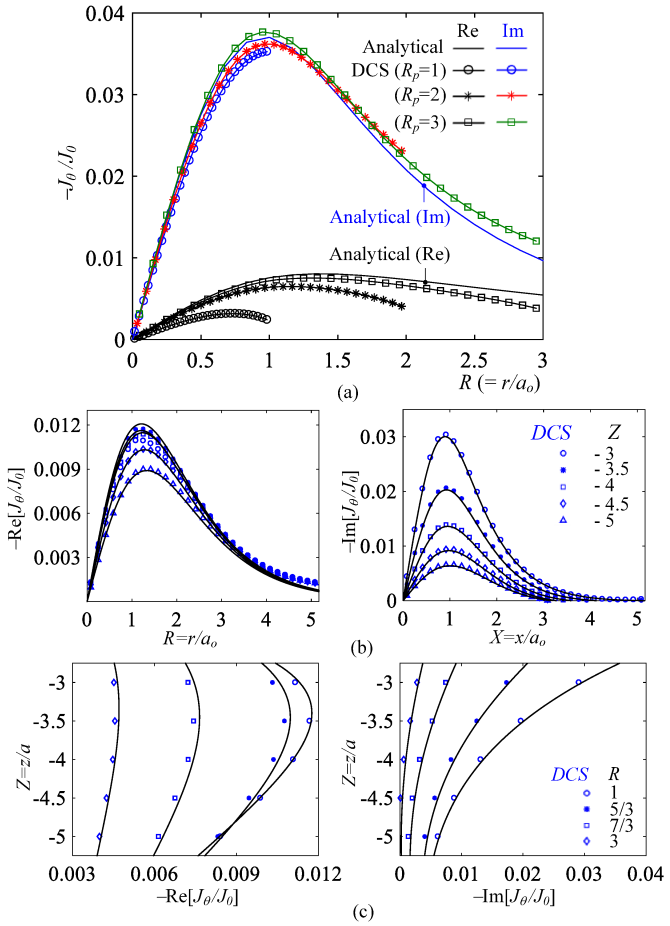

Fig. 5 Tangential ECD fields (H_p=2.5; Z_p = 2.75). (a) Boundary effect on real and imaginary parts of tangential ECD (Z= −5). (b) J_θ along the radial direction at a specified depth (R_p = 5). (c) J_θ along z direction at a radial location (R_p = 5).

C. *Computational effectiveness of the DCS model*

The effectiveness (efficiency and accuracy) of the DCS model is numerically evaluated by comparing of the computed MFD of the induced ECD with results simulated by COMSOL (commercial FEA software) for a benchmark problem; both 2D and 3D FEA meshes are considered as shown in Figs. 6(a, b). FEA models mesh all domains assuming both the nonferrous metallic plate (σ=10^5~10^8 Sm^{-1}) and the air (σ=1 S m^{-1}) are conductive to compute the MFD due to the induced ECD. For the benchmark problem, an annular EM is perpendicular to a non-ferrous square (72×72 mm^2) plate with a MFD sensor placed along the coil axis (x = y = 0) but 1mm above the plate. Because of the symmetry, the MFD ($|B_x|$, $|B_y|$) components of the induced circular eddy-currents are theoretically equal to zero; this observation provides a rational means to verify the solutions and a means to determine an appropriate number of elements needed in the DCS and FEA models. With the parametric values listed in Table 1 EM, Figs. 6(c, d) plot the ECD-induced MFD at the sensor location (R_s=0, Z_s=–2.25) computed using different number of elements.

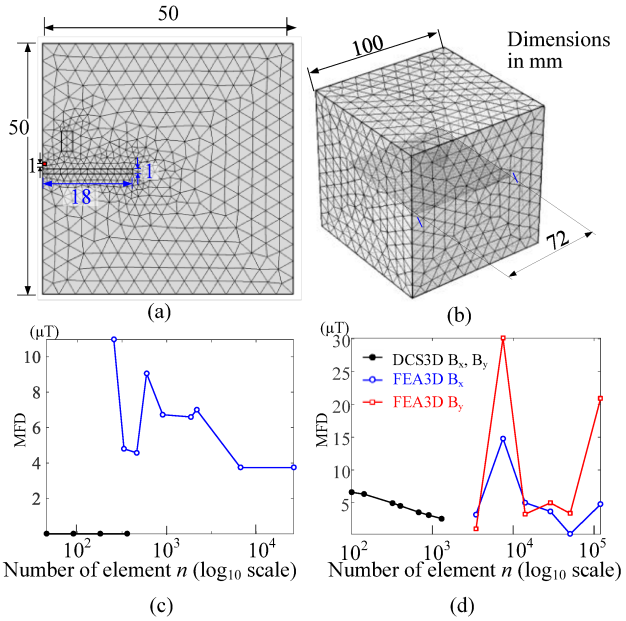

Fig. 6 Performance evaluation of the DCS model. (a) FEA 2D Mesh. (b) FEA 3D Mesh. (c) r component MFD. (d) x, y component MFD.

Table 1 and Fig. 6 offer some intuitive insights into the modeling of the MFD generated by the induced ECD:

– Table 1 shows that all the DCS and FEA models (2D or 3D) converge to a nearly identical $|B_z|$ value but the 2D $|B_r|$ or the 3D ($|B_x|$, $|B_y|$) components vary somewhat. As expected theoretically, the results show that $|B_r|$ of the 2D DCS model is zero and that the ($|B_x|$, $|B_y|$) computed from the 3D DCS model approaches zero as the number of elements increases (Fig. 6d). This validates both the 2D and 3D DCS models.

– The large area or volume of air space in the FEA models results in significant "quantitation noise" observed simulated MFD; as a result, both the 2D and 3D FEA yield non-zero $|B_r|$ or ($|B_x|$, $|B_y|$). This theoretically explains why FEA needs more elements to converge, and exhibits larger fluctuations with the number of elements for all cases in Figs. 6(c, d). Unlike FEA models, the DCS method (that uses point sources in direct modeling without the need to include the air space) results in more accurate but less variations in the MFD computation.

The DCS modeling method solves the pair of CLS problems, (19) and (20), where the number of elements (and hence the matrix sizes) represent a trade-off between its computational

1083-4435 (c) 2017 IEEE. Personal use is permitted, but republication/redistribution requires IEEE permission. See http://www.ieee.org/publications_standards/publications/rights/index.html for more information.

This article has been accepted for publication in a future issue of this journal, but has not been fully edited. Content may change prior to final publication. Citation information: DOI 10.1109/TMECH.2017.2771763, IEEE/ASME Transactions on Mechatronics

time and accuracy. Based on several n (= 2×2, 5×5, 10×10, 20×20, 30×30, and 40×40) elements, the computational time of the DCS modeling method is proportional to $n^{2.53}$. As a rule of thumb, the calculations with a PC (Intel Core *i*7-3630QM, 2.40GHz CPU, 16GB RAM, 64 bits OS) take about 14.1 seconds for a 20×20-element DCS model and 1 minutes for a 30×30-element DCS model.

IV. Experimental Results and Discussions

Three experiments were conducted to validate the DCS models and evaluate the MFD-based eddy-current (EC) sensor system [6] using the experimental setup as shown Fig. 7(a). The *first* experimentally validates the axisymmetric DCS model by comparing with the measured magnitude/phase of the MFD generated by the induced ECD in a 24mm-diameter 5.38mm-thick annular copper that has an electrical conductivity σ=58.4 MSiemens/m (or MS/m). The *second* investigates the boundary effects on the measured MFDs as the ECD sensor horizontally scans across an edge of an Aluminum plate. The *third* demonstrates the DCS method for modeling an ECD and measuring its MFD.

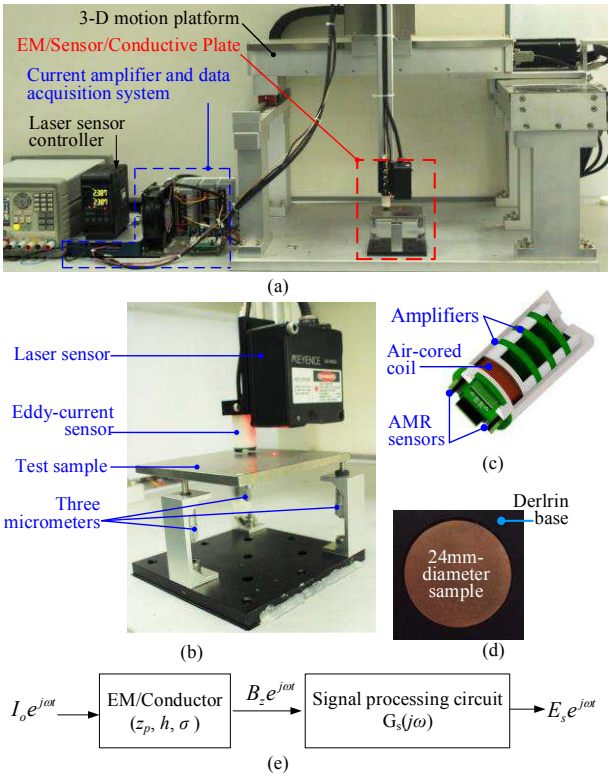

Fig. 7 Experimental setup. (a) Experimental testbed. (b) Measurement setup. (c) Eddy-current sensor. (d) Copper sample. (e) Sensor dynamics.

As shown in Figs. 7(a, b), the EC sensor is positioned by a three degree-of-freedom (DOF) precision translation stage with a laser-sensor above the test-sample. The test-sample relative to the magnetic sensor can be fine-tuned by three micrometers and the laser-sensor so that it is parallel to the sensor *xy*-plane. A pair of commercial (HMC1051) anisotropic magnetic resistance (AMR) sensors $S_{\pm}$ housed in the EM was used to measure the *z*-MFD from which the contribution of the pre-calibrated EM was subtracted from the measurements. As shown in Fig. 7(c), the AMR sensors are symmetrically placed near the outer radius of the coil where its *z*-MFD is minimum to avoid sensor saturation. Fig. 7(e) schematically illustrates the overall system dynamics, where the EM/conductive-plate system dynamics can be determined by the DCS model in terms of the parameters (Δ, z_p, h_p). The sensor dynamics (contributed by the signal processing amplifiers and associated circuits) are accounted for the transfer function $G_s(j\omega) = |G_s(j\omega)| \angle G_s(j\omega)$ in the 2nd block. The sensor system dynamics were determined to be 1.33 and –0.014° using a least-square (LS) method described in Appendix C. The parametric values of the EM, test samples and AMR sensor specifications, along with the operating frequencies, are detailed in Table II. The results for the three experiments are summarized in Figs. 8, 9 and 10.

A. Harmonic analysis of the 2D axisymmetric DCS model

Figure 8 shows the effects of the normalized skin-depth Δ defined in (17) and the normalized EM-plate distance Z_p on the ECD-generated MFD computed using a 2D axis-symmetrical DCS model with two different types of grid divisions; uniform grids and refined grids based on equal current density. To provide quantitative comparisons, the computed results are compared with experimentally measured magnitudes and phases of the copper sample shown in Fig. 7(d). As shown in Fig. 8, the magnitudes (left plot) depend on both Δ and Z_p but the phases are insensitive to Z_p. The % mean-squared-errors (MSEs) of the magnitudes computed using uniform and refined grids (relative to measurements) are 1.11×10^{-4} and 1.62×10^{-7} respectively. The corresponding MSEs of the phases are 0.0012 and 4.1712×10^{-4}. The discrepancies in the uniform DCS grids primarily occur at small Δ, where the refined grid method plays an important role to improve the computational effectiveness.

TABLE II. Parametric Values of Experimental Setup

EM Coil (N_w = 60, d_w = 0.35 mm) (a_i, a_o, a) = (3.75, 6, 2) mm I_o=1A, B_o= 16.67 μT		**AMR Sensor** (HMC1051ZL) Size: 6.5×1.7×2.0 mm $S_{\pm}$ (x_s, y_s, z_s): (±6, 0, –4.5) mm
Sensor system dynamics: $\lvert G_s(j\omega)\rvert$ = 1.33, $\angle G_s(j\omega)$ = –0.0141°		
Copper (Cu) σ = 58.4 MS/m h = 5.38 mm f=100Hz – 25kHz	**Titanium (Ti)** σ = 0.59 MS/m, h=5.013 mm f=10 – 25 kHz	**Aluminum (Al)** σ=35.5 MS/m h = 1 mm; d_h = 6, 12, 15 mm f = 1 kHz
z_p=6.5, 7.5, 8.5, 9.5 mm		z_p=6.5 mm
Edge scan w_p = 48 mm Number of elements: 576		**Hole scan** w_p = 72 mm Number of elements: 769, 670, 689

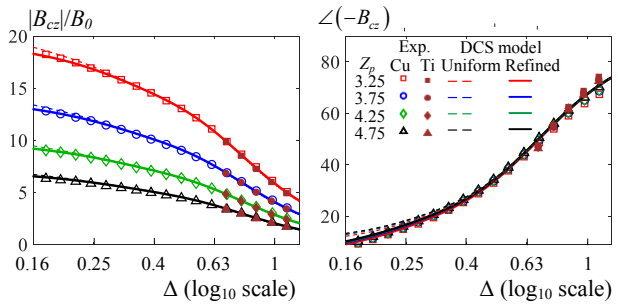

Fig 8. Experimental verification of the DCS model (single AMR)

Validated with experiments conducted on the two materials (copper and titanium alloy), the results confirm that the EC-induced and its corresponding MFD depends only on the

1083-4435 (c) 2017 IEEE. Personal use is permitted, but republication/redistribution requires IEEE permission. See http://www.ieee.org/publications_standards/publications/rights/index.html for more information.

This article has been accepted for publication in a future issue of this journal, but has not been fully edited. Content may change prior to final publication. Citation information: DOI 10.1109/TMECH.2017.2771763, IEEE/ASME Transactions on Mechatronics

normalized skin-depth (regardless of materials) for the specified pair of (H, Z_p). This finding is consistent with that reported in [24] for measurements with negligible edge effects.

B. Boundary effects on the DCS model

Figure 9(a) shows the state-space solutions of the eddy current field for experimentally investigating the edge effects on the MFDs measured by the pair of AMR sensors $S_{\pm}$ as the EC sensor moves horizontally across the Al plate from $X = -4$ to $X = 4$. The simulated and measured real and imaginary parts are compared in Fig. 9(b), and replotted in magnitudes and phases in Fig. 9(c).

To facilitate discussions, the path is divided into four stages:

Stage I $(X < -1)$: EM is outside the plate as S_+ approaches its left edge. No apparent edge effects are observed.

Stage II $(-1 \le X < 0)$: Less than half of the EM is above the plate. S_+ is above the plate. A sharp sign change in phase can be observed in S_- as the EM center approaches the left edge of the plate.

Stage III $(0 \le X < 1)$: More than half of the EM is above the plate as S_- approaches its left edge with S_+ above the plate.

Stage IV $\left(1 \le X < \frac{w_p}{a_o} - 4\right)$: EM (with both $S_{\pm}$) is completely above the plate. Apparent edge effects slowly disappear as the EC moves away from the edge.

Because the magnitudes in Stages I and II are infinitesimally small, the corresponding phases are difficult to measure accurately and thus the experimental phase data are ignored. Some intuitive insights can be gained from Fig. 9:

- As compared in Fig. 9(b) that graphs their real and imaginary parts, the measured MFDs agree well with the simulation validating the DCS model.
- The AMR sensor S_+ registers a smooth S-shape curve. However, a peak near $X = 1$ (where S_- is directly above the left edge) can be observed in both the real and imaginary parts in the S_- measurements.
- The phenomena of the S_- measurements can be explained with the aid of Fig. 9(d): As S_- approaches the edge from the far left, the positive EC ($+y$ direction in the cross sectional view) primarily contributed to positive B_{cz} (which increases until S_- is at the edge. As S_- passes the edge, the negative EC increases its contribution to the measured B_{cz}, causing it (and thus the phase) to change from positive to negative when S_- is directly above the edge, which is a meaningful phenomenon for edge detection.
- The above findings demonstrate that the number of sensors and their placement play an important role in edge localization.

C. Geometrical effects on ECD and its corresponding MFD

Fig. 10 illustrates the solutions to the DCS models in state-space representation for analyzing the M/EC fields of a plate that has a through hole (diameter d_h). The relatively complicated shape of the plate/hole configuration was geometrically modeled using a commercial CAD software Solidworks, and then discretized using a mesh generation software to create divisions (represented by nodes and elements) of irregular hexahedrons. Fig. 10(a) shows a typical hexahedron where the volume, areas and surface normal are given in Appendix B for completeness. Figures 10(b) and 10(c) show the typical DCS modeled EC fields induced in the plate when the EM is above the hole-center and at an offset along a radial path. Figures 10(d) to 10(f) compare the measured and simulated MFDs (where the data were determined at an interval of 1 mm) as the EC sensor swept over the hole (d_h = 6, 12, 15mm) along a radial path.

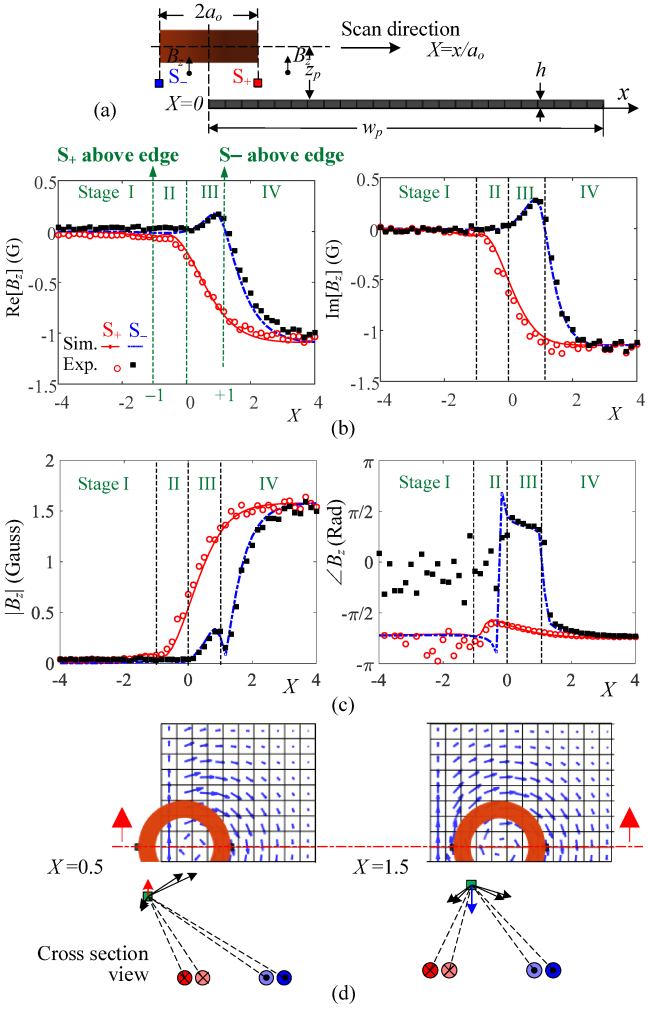

Fig. 9 Effect of edge boundary on z-component MFD. (a) Configuration. (b) Real and imaginary parts. (c) Magnitude and phase. (d) ECD and schematics illustrating edge-effect on measured MFD.

The following can be observed from the results:

- The experimental curves share similar trends with the simulation. The curves obtained from two AMR sensors are approximately symmetric about $X = 0$.
- Unlike Fig. 9 where S_+ registers a smooth S-shape magnitude curve between $X = -1$ and 1, S_+ experiences a local peak as it moves pass the edge of a hole. The shape of the magnitude curve around the peak depend on d_h/a_o.
- The resolution of the meshes could have a significant effect on numerical error. This is numerically illustrated in the zoom-in Fig. 10(g) where (3, 2.5 and 2) denote the three approximate global element-sizes in mm

1083-4435 (c) 2017 IEEE. Personal use is permitted, but republication/redistribution requires IEEE permission. See http://www.ieee.org/publications_standards/publications/rights/index.html for more information.

This article has been accepted for publication in a future issue of this journal, but has not been fully edited. Content may change prior to final publication. Citation information: DOI 10.1109/TMECH.2017.2771763, IEEE/ASME Transactions on Mechatronics

corresponding total numbers of elements (689, 938 and 1525). Due to the symmetry, the effects on the MFDs measured by S_+ were compared. As shown in Fig. 10(g), the local noisy peaks disappear when the meshes are sufficiently fine.

– The results show that the peaks of the three curves are at $X = -0.5$, 0 and 0.33 respectively, which correspond to the locations when S_+ is directly above the edge of the hole. The close agreements between the measured and simulated MFDs validate the DCS methods, and demonstrate its effectiveness for analyzing the M/EC fields of a configuration with a relatively complicated shape.

V. Conclusion

A distributed current source (DCS) modeling method for analyzing the magnetic and eddy-current fields of an eddy-current-based sensing system in state-space representation has been formulated. In harmonic forms, the eddy-current field is numerically solved for its real and imaginary parts as a two-step CLS problem subjected to the geometrical constraints imposed by the continuity equation and the object boundary conditions.

As demonstrated numerically, the efficiency/accuracy of the EC solutions can be improved without significantly increasing the number of elements, particularly for materials with a very small skin-depth, by appropriately distributing the grids based on the skin-depth effects. The DCS-based models have been numerically verified by comparing results with the 2D analytical axisymmetric solutions and FEA simulations; both 2D and 3D configurations are considered. The DCS models that account for the boundary effects of the object agree well with the 2D axisymmetric solution when $R_p \geq 3$ but the discrepancy increases for smaller R_p since the latter does not account for the boundary effects. Unlike FEA that requires a sufficiently large air space to enclose all the magnetic fields of both the EM and EC to ensure its solution accuracy, the DCS based models do not need to include the air space resulting in more accurate but less variations in the MFD computation.

The DCS-based EC models and their applications have been evaluated experimentally using measured MFDs, which involve three materials (copper, aluminum and titanium), and three object configurations (a semi-infinite conducting slab, an edge model and a plate with a through hole). The experimentally obtained frequency responses (with copper and titanium) suggest that the 2D axisymmetric solutions depend only on plate thickness, sensor-to-plate distance, and skin-depths. The close agreements between the DCS method and experiments confirm that the method is capable of handling the boundary effects of the object with complicated shapes, and offering high-fidelity physically intuitive predictions without sacrificing technical details. The DCS modeling method can be adapted for a spectrum of applications in robotics, mechatronics and industrial processes, where eddy current effects play an essential role. Applications may include design analysis of eddy-current sensors (for localization, geometrical measurement, defect detection and structural health monitoring) and actuators for the vibration suppression.

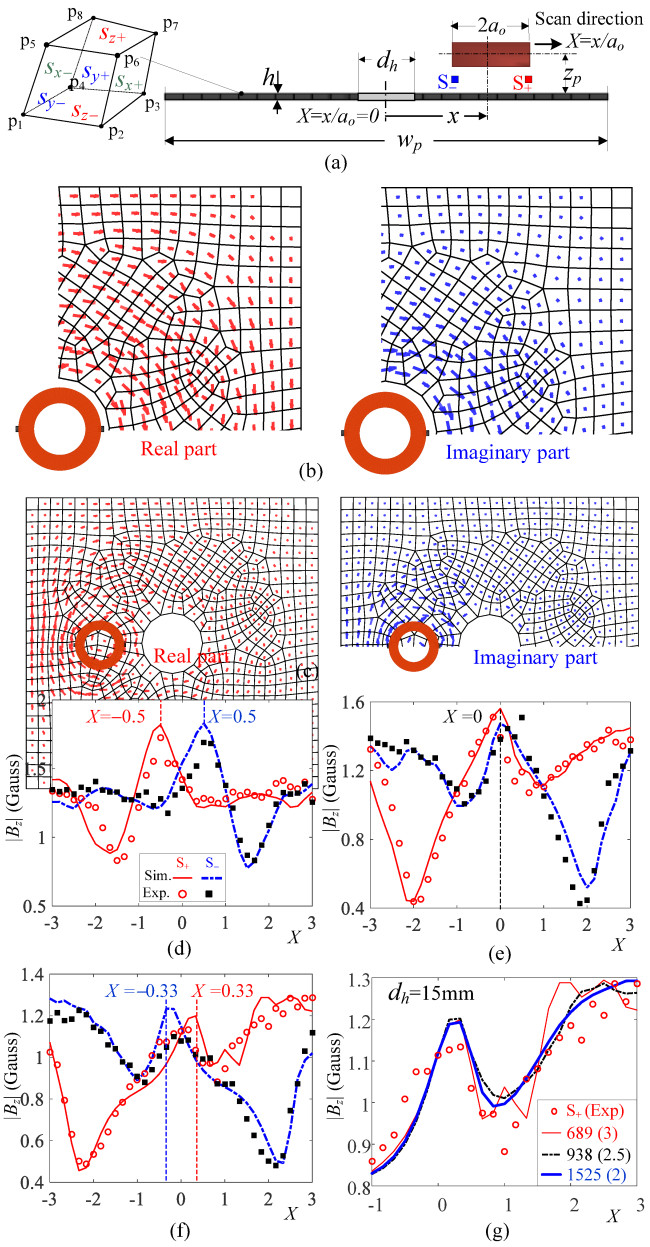

Fig. 10 Effect of hole on ECD and z-component MFD. (a) EM/Hole configuration and hexahedron elemental volume. (b) EC distribution at X=0 (right upper quadrant). (c) EC distribution at X= –3 (upper half). (d) d_h=6mm. (e) d_h=12mm. (f) d_h=15mm. (g) Effect of element resolution.

Appendix A
Biot-Savart Law

For applications where the effects of displacement current can be neglected, the Maxwell's equations that relate the magnetic and electric fields are given by (A.1a, b) along with the constitutive relations in (A.1c, d):

$$\nabla \times \mathbf{H} = \mathbf{J};\ \nabla \times \mathbf{E} = -\partial \mathbf{B} / \partial t;\ \mathbf{B} = \mu_o \mathbf{H} \text{ and } \mathbf{J} = \sigma \mathbf{E} \qquad \text{(A.1a~d)}$$

In (A.1), $\mathbf{H}$ and $\mathbf{E}$ are the magnetic and electric field intensities respectively, $\mathbf{J}$ is the eddy-current density (ECD) induced by the time-varying magnetic fields of the EM and conductor elements; $\mathbf{B}$ is the magnetic flux density; and μ_o is the

1083-4435 (c) 2017 IEEE. Personal use is permitted, but republication/redistribution requires IEEE permission. See http://www.ieee.org/publications_standards/publications/rights/index.html for more information.

This article has been accepted for publication in a future issue of this journal, but has not been fully edited. Content may change prior to final publication. Citation information: DOI 10.1109/TMECH.2017.2771763, IEEE/ASME Transactions on Mechatronics

permeability of free space the EC density. Using the two fundamental magneto-static postulates that specify the divergence and curl of **B**, **B** can be expressed as the curl of the magnetic vector potential $\boldsymbol{\phi}$ defined by (A.2a) and has an integral form in (A.2b) where Ω denotes the volume of the electric conductor; and $\mathbf{r}'$ and $\mathbf{r}$ are the position vectors of the EM and the observation point respectively:

$$\mathbf{B} = \nabla \times \boldsymbol{\phi} \text{ where } \boldsymbol{\phi}(\mathbf{r},t) = \frac{\mu_0}{4\pi}\int_{\Omega} \frac{\mathbf{J}(\mathbf{r}',t)}{|\mathbf{r}-\mathbf{r}'|} dV \qquad \text{(A.2a,b)}$$

The ECD **J** in (A.1d) can be explicitly expressed in terms of $\boldsymbol{\phi}$ by substituting **B** from (A.2a) into (A.1b) leading to

$$\mathbf{E} = -\frac{\partial \boldsymbol{\phi}}{\partial t}; \text{ hence } \mathbf{J} = -\sigma \frac{\partial \boldsymbol{\phi}}{\partial t} \qquad \text{(A.3a,b)}$$

Using (A.2a), **B** (generated by the combined effects of the input current to the EM and eddy current induced in the conductor respectively) can be derived from the curl of $\boldsymbol{\phi}$ leading to the Biot-Savart's law:

$$\mathbf{B}(\mathbf{r}) = \frac{\mu_0}{4\pi}\int_{\Omega} \frac{\mathbf{J}(\mathbf{r}')\times(\mathbf{r}-\mathbf{r}')}{|\mathbf{r}-\mathbf{r}'|^3} dV \qquad \text{(A.4)}$$

APPENDIX B
CAD-BASED DCS MODEL FOR COMPLEX GEOMETRY

Figure 10(a) shows a hexahedron with eight vertexes (p_1-p_8) and six quadrilateral surfaces (s_k, k=$x_{\pm}$, $y_{\pm}$, $z_{\pm}$) for analyzing the M/EC fields of irregular shape objects. The object geometry is described by the CAD and its discretized divisions are created by a mesh generation software. With the aid of Fig. 10(a) and Table B.1, the area s and the normal vector n of each hexahedron and its volume v are given by (B.1) to (B.3):

$$s_{\ell} = 0.5\left(|\mathbf{p}_{\ell 2}-\mathbf{p}_{\ell 1}|\times|\mathbf{p}_{\ell 4}-\mathbf{p}_{\ell 1}| + |\mathbf{p}_{\ell 2}-\mathbf{p}_{\ell 3}|\times|\mathbf{p}_{\ell 4}-\mathbf{p}_{\ell 3}|\right) \qquad \text{(B.1)}$$

$$\mathbf{n}_{\ell} = \frac{(\mathbf{p}_{\ell 2}-\mathbf{p}_{\ell 1})\times(\mathbf{p}_{\ell 3}-\mathbf{p}_{\ell 1})}{|(\mathbf{p}_{\ell 2}-\mathbf{p}_{\ell 1})\times(\mathbf{p}_{\ell 3}-\mathbf{p}_{\ell 1})|}, \text{ where } \ell = x_{\pm}, y_{\pm}, z_{\pm} \qquad \text{(B.2)}$$

$$v = \frac{1}{2}\sum_{ti=1}^{6}\left\{(\mathbf{p}_{ti,4}-\mathbf{p}_{ti,1})\bullet\left[(\mathbf{p}_{ti,2}-\mathbf{p}_{ti,1})\times(\mathbf{p}_{ti,3}-\mathbf{p}_{ti,1})\right]\right\} \qquad \text{(B.3)}$$

In (B.1) and (B.2), the vertexes $\mathbf{p}_{\ell i}$ (where i=1, 2, 3 and 4) for the ℓ quadrilateral surface (made of two triangles) are tabulated on the left side of Table B.1. Equation (B.3) sums the six tetrahedron volumes (denoted as t_i =1 to 6) that make up the hexahedron, where $\mathbf{p}_{ti,i}$ are listed on the right side of Table B.1.

TABLE B.1. VERTEXES OF TETRAHEDRONS AND SURFACES

ℓ	$\mathbf{p}_{\ell 1}$	$\mathbf{p}_{\ell 2}$	$\mathbf{p}_{\ell 3}$	$\mathbf{p}_{\ell 4}$	t_i	$\mathbf{p}_{ti,1}$	$\mathbf{p}_{ti,2}$	$\mathbf{p}_{ti,3}$	$\mathbf{p}_{ti,4}$
$x+$	$\mathbf{p}_2$	$\mathbf{p}_3$	$\mathbf{p}_7$	$\mathbf{p}_6$	t_1	$\mathbf{p}_1$	$\mathbf{p}_2$	$\mathbf{p}_4$	$\mathbf{p}_5$
$x-$	$\mathbf{p}_1$	$\mathbf{p}_5$	$\mathbf{p}_8$	$\mathbf{p}_4$	t_2	$\mathbf{p}_5$	$\mathbf{p}_4$	$\mathbf{p}_8$	$\mathbf{p}_6$
$y+$	$\mathbf{p}_3$	$\mathbf{p}_4$	$\mathbf{p}_8$	$\mathbf{p}_7$	t_3	$\mathbf{p}_5$	$\mathbf{p}_6$	$\mathbf{p}_2$	$\mathbf{p}_4$
$y-$	$\mathbf{p}_1$	$\mathbf{p}_2$	$\mathbf{p}_6$	$\mathbf{p}_5$	t_4	$\mathbf{p}_3$	$\mathbf{p}_7$	$\mathbf{p}_8$	$\mathbf{p}_6$
$z+$	$\mathbf{p}_5$	$\mathbf{p}_6$	$\mathbf{p}_7$	$\mathbf{p}_8$	t_5	$\mathbf{p}_2$	$\mathbf{p}_3$	$\mathbf{p}_4$	$\mathbf{p}_6$
$z-$	$\mathbf{p}_1$	$\mathbf{p}_4$	$\mathbf{p}_3$	$\mathbf{p}_2$	t_6	$\mathbf{p}_4$	$\mathbf{p}_3$	$\mathbf{p}_8$	$\mathbf{p}_6$

APPENDIX C
LEAST SQUARE ESTIMATION OF SENSOR PARAMETER [6]

The dynamics of the MFD measurement/signal-processing electronics is accounted for by the transfer function (C.1) where (M, P) denote (magnitude, phase):

$$G_S(j\omega) = M_s \angle P_S \qquad \text{(C.1)}$$

With the measured (M_E, P_E) of the overall system and experimentally identified sensor (without the conductor), the EM/Conductor system can be estimated in real time:

$$\tilde{M}_B = M_E M_S^{-1} \text{ and } \tilde{P}_B = P_E + (-P_S) \qquad \text{(C.2)}$$

The parameters (M_S, P_S) that characterize the electronic system dynamics are calibrated by minimizing the error function E:

$$E = \sum_{i=1}^{m}\left[\left(M_{Ei} - M_S M_{Bi}\right)^2 + \left(P_{Ei} - P_{Bi} - P_S\right)^2\right] \qquad \text{(C.3)}$$

Minimizing E by solving $\partial E/M_S$=0 and $\partial E/P_S$=0 lead to

$$M_S = \sum_{i=1}^{m}\left(M_{Ei}M_{Bi}\right) / \sum_{i=1}^{m} M_{Bi}^2 \text{ and } P_S = \frac{1}{m}\sum_{i=1}^{m}\left(P_{Ei} - P_{Bi}\right). \qquad \text{(C.4)}$$

REFERENCES

[1] K.-M. Lee, M. Li and K. Bai, "An investigation of eddy-current effects on parameter monitoring for duplex lathe machining of thin-wall components," *ASME Dynamic Systems and Control Conf*., San Antonio, Texas, USA. Oct. 22-24, 2014, DSCC2014-6193.

[2] S. C. Chen, H. S. Peng, J. A. Chang, and W. R. Jong, "Simulations and verifications of induction heating on a mold plate," *International Communications in Heat and Mass Transfer*, vol. 31, no. 7, pp. 971–980, Oct. 2004.

[3] J.-S. Bae, M. K. Kwak, and D. J. Inman, "Vibration suppression of a cantilever beam using eddy current damper," *Journal of Sound and Vibration*, vol. 284, pp. 805–824,Jun. 2005

[4] M. R. Nabavi, S. N. Nihtianov, "Design strategies for eddy-current displacement sensor systems: review and recommendations," *IEEE Sensors Journal*, vol. 12, no. 12, pp. 3346–3355, Dec. 2012.

[5] A. Devillez and D. Dudzinski, "Tool vibration detection with eddy current sensors in machining process and computation of stability lobes using fuzzy classifiers," *Mechanical Systems and Signal Processing,* vol. 21, no. 1, pp. 441-456, Jan. 2007.

[6] K.-M. Lee, C.-Y. Lin, M. Li, and B. J. Hao, "Harmonic response of an eddy-current sensor for real-time measurement of thin-wall Titanium alloy workpiece," in *Proc. IEEE/ASME Int. Conf. on Adv. Intelli. Mechatronics*, *2016,*, pp. 1271-1276.

[7] F. Sakran, M. Golosovsky, H. Goldberger, and D. Davidov, "High-frequency eddy-current technique for thickness measurement of micron-thick conducting layers," *Applied Physics Letters*, vol. 78, no. 11, pp. 1634-1626, Jan. 2001.

[8] John C. Moulder, Erol Uzal, and James H. Rose1, "Thickness and conductivity of metallic layers from eddy current measurements," *Review of Scientific Instruments*, vol. 63, no. 6, pp. 3455-3465, Jan.,1992.

[9] X. Ma, and A. J. Peyton, "Eddy current measurement of the electrical conductivity and porosity of metal foams," *IEEE Trans. on Instrumentation and Measurement*, vol. 55, no. 2, pp 570-576, Mar., 2006.

[10] B. A. Abu-Nabah and P. B. Nagy, "High-frequency eddy current conductivity spectroscopy for residual stress profiling in surface-treated nickel-base superalloys," *NDT & E International*, vol. 40, no. 5, pp. 405-418, Feb., 2007.

[11] C. V. Dodd and W. E. Deeds, "Analytical solutions to eddy-current probe-coil problems," *J. Appl. Phys*., vol. 39, pp. 2829-2838, May, 1968.

[12] G. Sinha and S. S. Prabhu, "Analytical model for estimation of eddy current and power loss in conducting plate and its application," *Physical Review*, vol.14, 0624201, Jun., 2011.

[13] J. T. Jeng, H. E. Horng, H.C. Yang, J. C. Chen, and J. H. Chen "Simulation of the magnetic field due to defects and verification using high-Tc SQUID, " *Physica C*, pp 298-302, Feb., 2002.

[14] T. P. Theodoulidis, and J. R. Bowler, "The truncated region eigenfunction expansion method for the solution of boundary value problems in eddy current nondestructive evaluation," *in Proc. of American Institute of Physics*, vol. 760, pp. 403-408, 2005.

1083-4435 (c) 2017 IEEE. Personal use is permitted, but republication/redistribution requires IEEE permission. See http://www.ieee.org/publications_standards/publications/rights/index.html for more information.

This article has been accepted for publication in a future issue of this journal, but has not been fully edited. Content may change prior to final publication. Citation information: DOI 10.1109/TMECH.2017.2771763, IEEE/ASME Transactions on Mechatronics

[15] T. Theodoulidis and E. Kriezis, "Series expansions in eddy current nondestructive evaluation models," *J. of Materials Processing Technology*, vol. 161, pp. 343-347, Jul., 2005.

[16] N. D. Geeter, G. Crevecoeur, and L. Dupre, "An efficient 3-D eddy-current solver using an independent impedance method for transcranial magnetic stimulation," *IEEE Trans. on Biomedical Engineering*, vol. 58, No. 2, pp. 310-320, Oct., 1984.

[17] N. D. Geeter, G. Crevecoeur, and L. Dupre, "Eddy-current simulations using an independent impedance method in anisotropic biological tissues," *IEEE Trans. on Magnetics*, vol. 47, No. 10, pp. 3845-3848, Oct., 2011.

[18] O. P. Gandhi, J. F. DeFord, and Hiroshi Kanai, "Impedence method for calculation of power deposition patterns in magnetically induced Hypertherimia," *IEEE Trans. on Biomedical Engineering*, vol. 31, No. 10, pp. 644-651, Oct., 1984.

[19] N. Orcutt, and O. P. Gandhi, "A 3-D impedance method to calculate power deposition in biological bodies subjected to time varying magnetic fields," *IEEE Trans. on Magnetics*, vol. 46, No. 4, pp. 1034-1041, Apr., 2010.

[20] P. Alotto, P. Bettini, and R. Specogna, "Sparsification of BEM matrices for large-scale eddy current problems," *IEEE Trans. on Magnetics*, vol. 52, No. 3, pp. 1-4, Apr., 2016.

[21] K.-M. Lee and H. Son, "Distributed multipole model for design of permanent-magnet-based actuators, " *IEEE Trans. on Magnetics*, vol. 43, no. 10, pp. 3904-391, Oct., 2007.

[22] K.-M. Lee, K. Bai, and J. Y. Lim, "Dipole models for forward/inverse torque computation of a spherical motor," *IEEE/ASME Trans. on Mechatronics*, vol. 14, no. 1, pp 46-54, Feb. 2009.

[23] J. Y. Lim, and K.-M. Lee, "Distributed multilevel current models for design analysis of electromagnetic actuators," *IEEE/ASME Trans. on Mechatronics*, vol. 20, no. 5, pp 2413-2424, Oct. 2015.

[24] K.-M. Lee, C.-Y. Lin, B. Hao, and M. Li, "Coupled parametric effects on magnetic fields of eddy-current induced in non-ferrous metal plate for simultaneous estimation of geometrical parameters and electrical conductivity" *IEEE Trans. on Magnetics*, DOI 10.1109/TMAG.2017. 2715831, 2017.

[25] K.-M., Lee. L. Yang, K. Bai, and J. Ji, "An efficient flexible division algorithm for predicting temperature-fields of mechatronic system with manufacturing applications," *IEEE/ASME Trans. on Mechatronics*, vol. 22, August 2017, pp 1818-1827.

Chun-Yeon Lin received the B.S. degree in mechanical engineering from National Central University, Taoyuan, Taiwan, in 2003; the M.S. degree in electrical control engineering from National Chiao-Tung University, Hsinchu, Taiwan, in 2005; and the M.S. degree in mechanical engineering from Stanford University, Stanford, CA, USA, in 2009. He is currently working toward the Ph.D. degree at the George W. Woodruff School of Mechanical Engineering, Georgia Institute of Technology, Atlanta, GA, USA.

His current research interests include mechatronics, physical modelling, machine vision, electromagnetic and intelligent system.

Kok-Meng Lee (M'89–SM'02–F'05) received the B.S. degree from the State University of New York, Buffalo, NY, USA, in 1980, and the S.M. and Ph.D. degrees from the Massachusetts Institute of Technology, Cambridge, MA, USA, in 1982 and 1985, respectively. He is currently a Professor in the George W. Woodruff School of Mechanical Engineering, Georgia Institute of Technology, Atlanta, GA, USA. He was also honored as Pao Yu-Kong Chair Professor at Zhejiang University. He is also Distinguished Professor with the State Key Laboratory of Digital Manufacturing Equipment and Technology, Huazhong University of Science and Technology, Wuhan, China, under the National Recruitment Program of Global Experts.

His current research interests include system dynamics/control, robotics, automation, and mechatronics. He holds eight patents in machine vision, a three-degrees-of-freedom (DOF) spherical motor/encoder, and a live-bird handling system.

Dr. Lee is a Fellow of the ASME. He received the National Science Foundation (NSF) Presidential Young Investigator, Sigma Xi Junior Faculty Research, International Hall of Fame New Technology International Hall of Fame New Technology, Kayamori Best Paper award, and TMech Best Paper award.

Bingjie Hao received the B.S. degree in Mechanical Engineering from the Huazhong University of Science and Technology (HUST), Wuhan, China in 2014. He is currently working toward the Ph.D. degree in Mechanical Engineering, and Research Assistant in the State Key Laboratory of Digital Manufacturing Equipment and Technology, HUST.

His research interests include mechatronics electromagnetics, sensors and control.

1083-4435 (c) 2017 IEEE. Personal use is permitted, but republication/redistribution requires IEEE permission. See http://www.ieee.org/publications_standards/publications/rights/index.html for more information.